RSC Advances

ROYAL SOCIETY OF CHEMISTRY

PAPER

View Article Online
View Journal | View Issue

Cite this: *RSC Adv.*, 2026, **16**, 19743

Abundant oxygen vacancies assisting $NaPO_3$ supported by porous carbon derived from cotton pulp black liquor as a transition metal-free electrocatalyst for efficiently enhancing the urea oxidation reaction

Zhuoyan Liu,†[ab] Haowen Li,†[ab] Zhenming Li,[a] Yixin Zheng,[a] Raojie Liao,[a] Jianfeng Li,[a] Lijun Wang,[c] Jianhui Jiang,[ab] Libing Hu *[ab] and Jianbo Zhao *[ab]

Received 5th February 2026
Accepted 28th March 2026

DOI: 10.1039/d6ra01021k

rsc.li/rsc-advances

To improve green hydrogen production and to significantly treat urea-rich wastewater, exploring transition-metal-free electrocatalysts with high performance for the urea oxidation reaction (UOR) is significant but challenging. Herein, the acid precipitation method is used to extract biomass from cotton pulp black liquor (CPBL) using different H_3PO_4 treatments to regulate the pH values (pH = 1, 7 and 11). The as-obtained biomass containing sodium salts is employed to prepare the electrocatalysts after high-temperature treatment, and they are named PCMA-*x* (*x*: pH = 1, 7 and 11). The physical characterizations confirm that the electrocatalysts are composed of porous carbon and $NaPO_3$, and typically, PCMA-7 has the highest oxygen vacancies. Experimental results confirm that PCMA-7 delivers the highest electrocatalytic UOR activity with the lowest overpotential of 132 mV and the lowest Tafel slope of 33.8 mV dec^{-1}. Based on physical characterizations, experimental results, and DFT calculations, it is clearly found that PCMA-7 exhibits a superior catalytic UOR efficiency because the porous structure provides a channel for ion transport/electrolyte transmission, abundant oxygen vacancies strengthen intermediate adsorption/activation, and $NaPO_3$ accelerates the reaction of key intermediates.

1. Introduction

With the consumption of traditional fossil fuels excessively increasing, the energy crisis and environmental pollution are becoming increasingly severe, which has inevitably threatened human life.[1] Accordingly, it is urgent to develop alternative energy resources. Among them, hydrogen has its inherent merits of cleanliness, renewability, and high energy density, so it is considered one of the most promising alternatives to fossil fuels.[2] To date, coal gasification, steam reforming and electrocatalytic water splitting have developed as the three main routes for producing hydrogen. In comparison with coal gasification and steam reforming, electrocatalytic water splitting has been regarded as a promising method for hydrogen production.[3–6] Nevertheless, the practical performance of electrocatalytic water splitting is remarkably limited by the kinetically sluggish charge transfer of the oxygen evolution reaction (OER) at the anode.[7] The replacement of OER with thermodynamically favorable organic oxidation reactions can reduce the anodic overpotential and thus has attracted enormous attention.[8] Nowadays, electrocatalytic oxidation reactions of small organic molecules at the anode, such as methanol oxidation reaction (MOR), furfural oxidation reaction (FOR), and urea oxidation reaction (UOR), are widely employed to replace OER due to their low thermodynamic equilibrium potentials.[9,10] Among them, UOR has been extensively studied by virtue of its two main advantages: (1) the thermodynamic equilibrium potential of the UOR (0.37 V) is significantly lower than that of the OER (1.23 V); (2) electrocatalytic UOR can be used to treat urea-rich sewage for achieving the dual purpose of producing clean energy and solving environmental problems.[11–13] Unfortunately, the UOR process involves a complex six-electron transfer reaction and the undesirable adsorption/desorption of the corresponding intermediates, leading to the sluggish reaction kinetics of UOR.[14,15] Consequently, the practical application of UOR still encounters limitations. According to the above considerations, developing efficient UOR electrocatalysts is critical for the electrochemical treatment of urea-rich wastewater to produce green hydrogen.[16,17] To date, the state-of-the-art Ir- and Ru-based precious metal electrocatalysts have revealed superior

[a]*College of Chemistry and Chemical Engineering, Tarim University, Alaer 843300, P. R. China. E-mail: hlbin148@163.com; zjb1102@outlook.com*

[b]*Engineering Laboratory of Chemical Resources Utilization in South Xinjiang of Xinjiang Production and Construction Corps, Tarim University, Alaer 843300, P. R. China*

[c]*Analysis and Testing Center, Tarim University, Alaer 843300, P. R. China*

† These authors contributed equally to this work.

performance for UOR.[18] However, their high price and limited resources greatly impede their practical application.[19,20] Accordingly, it is crucial to produce high-performance non-noble metal catalysts for UOR with reduced energy consumption.

To date, significant efforts have been devoted to designing and producing a series of cost-effective and robust non-noble metal-based electrocatalysts for UOR, such as transition metal-based oxides, hydroxides, sulfides, phosphides, selenides, and others.[21,22] Based on these successful achievements, material scientists have explored other non-noble-metal electrocatalysts. Among them, metal-based phosphates and metaphosphates as electrocatalysts have attracted considerable attention recently because transition metal metaphosphates/phosphates are able to stabilize the intermediate states of the transition metal ions and provide positive contributions to structural stability.[21,23] In addition, experiments and theoretical studies provide evidence that the phosphate/metaphosphate groups deliver excellent contributions in proton migration, which plays a role of outstanding significance for catalysis.[24] To date, transition-metal metaphosphates (TMMPs) with phosphorus (P) have attracted extensive research interest because they hold potential as cost-effective OER catalysts.[25,26] In particular, different kinds of Fe-, Co-, and Ni-based metaphosphate electrocatalysts have been developed, and they show electrocatalytic OER properties. For example, Gond *et al.* reported that sodium cobalt metaphosphate $NaCo(PO_3)_3$ delivered a higher electrocatalytic OER activity than that of the commercial RuO_2 catalyst. It can arise because active sites were stabilized by the PO_4 units in its structure, while the Co centers provide the electrophilicity by virtue of the presence of phosphorus, which offers a prominently catalytic active center for OH^- adsorption.[27] Nevertheless, transition metal-free metaphosphates with high electrocatalytic activity towards UOR remain unexplored, and their mechanism is still unclear.

In addition, the electrocatalytic UOR performance of the pure metaphosphates is unsatisfactory. To improve the electrocatalytic performance of electrocatalysts, a general approach is to couple materials with carbon materials as conductive supports (including CNTs, graphene, and 3D foams) with high conductivity, which have been extensively studied to enhance the electrocatalytic performance.[28,29] For example, Liu *et al.* successfully loaded $Ni(PO_3)_2$ nanoparticles onto CNTs by using a combined process of self-assembly, pyrolysis, and phosphidation and successfully obtained the catalyst $Ni(PO_3)_2$/CNTs. They demonstrated that the as-prepared $Ni(PO_3)_2$/CNTs exhibited superior electrocatalytic HER performance, attributed to the maximum exposure of active sites by CNTs and the effective promotion of electron transfer.[30] Among various carbon materials, porous carbon materials, featuring a high specific surface area, tunable pore structure, and prominent electrical conductivity, are emerging as promising supports.[31,32] Research is now developing renewable precursors to prepare porous carbon.[33] In particular, cotton pulp black liquor (CPBL), as a byproduct, is produced in large quantities in the textile industry, posing a significant threat to aquatic and soil ecosystems. Notably, the main components of CPBL include dissolved cellulose, hemicellulose, and lignin. Accordingly, CPBL as a sustainable feedstocks for preparing porous carbon as a support for TMMPs for UOR not only offers a viable solution to address the environmental issues, but also improves the high-value application of CPBL. Besides supports playing an important role in UOR, oxygen vacancies can offer a large number of active centers and improve the conductivity of the electrocatalysts, which in turn promotes the bond dissociation of urea to enhance UOR.[34–37] Nevertheless, developing high-efficiency electrocatalysts with defect engineering in alkali metal metaphosphates usually involves complex and inconvenient preparation methods.[38,39] As a result, the dominant challenge remains in developing an alkali metal metaphosphate-based catalyst with abundant oxygen vacancies for high-performance UOR *via* an efficient and facile protocol. More importantly, their synergistic mechanism for electrocatalytic UOR remains unclear and needs to be explored.

Based on the above-discussion, the biomass (such as dissolved lignin, hemicellulose, cellulose) in CPBL was extracted using H_3PO_4, and then, their pH values (pH = 1, 7 and 11) were adjusted using H_3PO_4. As expected, $NaPO_3$ was formed *in situ* in porous carbon matrices (PCMA-1, PCMA-7, and PCMA-11) derived from biomass after high-temperature treatment, and meanwhile, oxygen vacancies were formed during the process. The porous structure served as the passageway for ion transport/electrolyte transmission, abundant oxygen vacancies strengthened intermediate adsorption/activation, and $NaPO_3$ accelerated the reaction of key intermediates, which were beneficial for the UOR performance.[40–42] Based on these merits, PCMA-7 exhibited superior electrocatalytic UOR activity with the lowest overpotential of 132 mV, and the lowest Tafel slope of 33.8 mV dec^{-1}. Density functional theory (DFT) calculations confirmed that PCMA-7 delivered the lowest energy barrier during the rate-determining step (RDS). This work not only offers a feasible approach to convert CPBL into high-value materials but also develops an efficient electrocatalyst to treat urea-rich wastewater.

2. Materials and methods

2.1 Materials

Reagents applied in this work are as follows: potassium hydroxide (KOH, A.R.), phosphoric acid (H_3PO_4, A.R.), hydrochloric acid (HCl, 36–38%), *n*-hexane (C_6H_{14}, A.R.), cyclopentane (C_5H_{10}, A.R.), ethyl acetate ($CH_3COOC_2H_5$, 99.9%), acetone (CH_3COCH_3, A.R.), and *n*-propanol (C_3H_7OH, chromatographic grade, 99.9%). All of them were sourced from Shandong Hui'an Chemical Co., Ltd. Cotton pulp black liquor (CPBL), which contained biomass resources such as lignin, cellulose, hemicellulose, and wax, was obtained from Alar Zhongtai Textile Technology Co., Ltd. All reagents were utilized as received without further processing.

2.2 Treatment of CPBL to obtain the biomass precipitate

The acid precipitation method was employed to extract biomass from CPBL using H_3PO_4 with pH adjustment (Fig. 1A). Typically,

a certain amount of CPBL was diluted with distilled water under magnetic stirring for 10 min. Subsequently, H_3PO_4 solution was added to adjust the pH to 1, 7 and 11 and stirred for 2 h. After that, the mixed solution was centrifuged at 5000 rpm. The obtained biomass precipitate was dried at 80 °C for 72 h. Finally, the dried sediment was ground in a high-speed pulverizer, and then a 60-mesh sieve was used to remove the large particles to obtain the biomass powder.

2.3 Preparation of porous carbon-supported $NaPO_3$

To obtain the desirable catalysts, biomass powders and KOH [1 : 1 (g/g)] were firstly mixed uniformly by grinding for 30 min. Then, the mixture was placed into a tube furnace and calcined in a nitrogen atmosphere at 400 °C for 6 h. After cooling down to room temperature, large particles were removed from the obtained products using a 60-mesh sieve. The porous carbons were named as PCMA-1, PCMA-7, and PCMA-11, respectively, according to the pH (Fig. 1B).

2.4 Materials characterization

The crystal phases of the catalysts were analyzed by X-ray diffraction (XRD, D8 Advance, Bruker) using Cu Kα radiation. Scanning electron microscopy (SEM) was performed using a Hitachi SU8020 instrument to characterize the surface microstructure and morphology of all electrocatalysts. The infrared spectra were recorded using a Nicolet iS10 FTIR Spectrometer from Thermo Fisher Scientific. The N_2 adsorption–desorption isotherms were recorded at −196 °C on an ASAP 2020 instrument. The specific surface areas (S_{BET}) of the catalysts were determined by the Brunauer–Emmett–Teller (BET) method. The pore size distribution was calculated by employing the Barrett–Joyner–Halenda (BJH) method according to the adsorption branch of the isotherms. All the X-ray photoelectron spectroscopy (XPS) spectra were obtained using an XPS equipment (Thermo Fisher ESCALAB 33.80Xi, USA) employing an Al Kα source with a constant voltage at 12.5 kV and a current of 16 mA. Typically, they were calibrated using the C 1s peak position of 284.8 eV acting as a reference. Raman analysis was performed using a Renishaw Raman spectrometer to characterize the state of carbon in the samples.

2.5 Preparation of working electrodes

Before the preparation of the working electrodes, nickel foam (NF, 1 cm × 1 cm), as the current collector, was cleaned in 0.1 M HCl using ultrasonic treatment for 30 min. Then, it was washed three times with acetone and deionized water, respectively, after which it was dried in a vacuum oven at 80 °C for 24 h. Subsequently, the catalyst inks were prepared by uniformly mixing 1 μL PTFE ethanol solution and 1 mg of catalyst powder (PCMA-1, PCMA-7, and PCMA-11 and IrO_2) followed by ultrasonic treatment for 30 min. After that, the as-obtained homogeneous inks were dropped on the as-cleaned NF substrate. Finally, the desirable working electrodes were obtained after they were dried at 80 °C for 24 h.

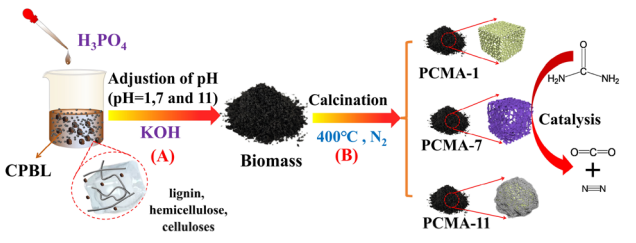

Fig. 1 Schematic route for the preparation of porous carbon-supported H_3PO_4 from CPBL.

2.6 Electrochemical measurements

All electrochemical UOR tests were conducted using a CHI-660E electrochemical workstation (Chenhua, Shanghai, China) according to a typical three-electrode system with platinum wire (the counter electrode), the Hg/HgO reference electrode and the as-obtained working electrode. Typically, all electrochemical UOR tests were performed through cyclic voltammetry (CV) after 20 cycles. The electrolyte solutions adopted for the tests were 1 M KOH + 0.33 M urea. Based on the following formula, the potentials were all calibrated to a reversible hydrogen electrode (RHE): $E_{RHE} = E_{Hg/HgO} + 0.098 + 0.0591 \times pH$. Moreover, the UOR performances of the different electrocatalysts were examined with polarization curves acquired by utilizing linear sweep voltammetry (LSV) with a scan rate of 5 mV s^{-1} after *iR* correction. Typically, the corresponding Tafel plots were extrapolated by fitting the linear portion between the potential (η) and the log current ($\log j$) based on the equation ($\eta = b \log j + a$), where b stands for the Tafel slope. In addition, the electrochemically active surface area (ECSA) was carefully evaluated by measuring the double-layer capacitance (C_{dl}) according to the linear relation between ECSA and C_{dl}. The C_{dl} were obtained by CV measurements at different scan rates (20, 40, 60, 80, and 100 mV s^{-1}) in the non-faradaic region. Typically, the electrochemical impedance spectroscopy (EIS) evaluations were carried out with the frequency ranging from 0.01 Hz to 100 kHz.

2.7 Computational details

All spin-polarized DFT calculations were carried out in the Vienna *ab initio* Simulation Package (VASP). The electron exchange–correlation potential was described by employing the Perdew–Burke–Ernzerhof (PBE) functional and the generalized gradient approximation (GGA) method. The ion–electron interactions were treated using the projector-augmented-wave (PAW) pseudopotential. A 5 × 5 × 1 Monkhorst–Pack *k*-point mesh was used to sample the Brillouin zone in the optimization of electrons and ions, and a plane-wave cutoff energy was fixed at 600 eV, until a force convergence of 0.02 eV $Å^{-1}$ and an energy convergence of 10^{-5} eV per atom were obtained for each atom under the conjugate gradient (CG) algorithm. Grimme's semi-empirical DFT-D3 method was applied to correct the Gibbs free energy to account for the van der Waals interactions between the substrate and the adsorbates. In addition, a 20 Å vacuum space was fixed along the *z*-direction to evade the interactions between different interlayers, which were yielded from the periodic boundary condition. Under ambient conditions, the

computational hydrogen electrode (CHE) model was utilized to correct the Gibbs free energy. Typically, the CHE was defined as the free energy change of a proton and electron pair transfer according to the following formula:

$$\Delta G = \Delta H + \Delta \mathrm{ZPE} \pm T\Delta S$$

where ΔH represents the reaction energy that can be obtained from DFT calculations, while ΔZPE and ΔS are the zero-point energy and the entropy change of each reaction step at 298.15 K, respectively.

3. Results and discussion

The morphologies and microstructures of the samples were examined using FE-SEM (Fig. 2a–f). In the low-magnification SEM images (Fig. 2a–c), it could be clearly seen that PCMA-1, PCMA-7, and PCMA-11 display porous structures. In order to clearly investigate them, their high-magnification SEM images are shown in Fig. 2d–f. In comparison with PCMA-1 and PCMA-11, PCMA-7 exhibited smaller pore size and thinner cellular wall, resulting in higher pore density. Some of the pores, especially the small ones, collapsed to result in large pores, confirming that the specific surface area increased and the pore sizes changed when it was pyrolyzed at high temperature with the addition of KOH. In addition, these pores are interconnected with each other to result in various channels, which was able to offer more space for electrolyte diffusion to boost the electrocatalytic performance. This structure provided a large specific surface area favorable for efficient mass transport and ion diffusion, making it particularly advantageous for electrochemical processes.[43] The abundant macropores enhanced electrolyte accessibility and promoted the rapid release of gas during catalytic activity, leading to improved reaction kinetics and a lower overpotential for UOR. The EDS mapping images further corroborated the homogeneous distribution of key elements (such as C, O, Na, and P) in PCMA-7. The homogeneous dispersion of Na and P affirmed the successful incorporation of sodium metaphosphate phases into the pore carbon, which are known to affect the catalytic performance by introducing active sites and improving the stability of the material during prolonged electrochemical reactions.

To assess the composition of the samples, XRD measurements were carried out. Obviously, the XRD patterns (Fig. 3a) revealed sharp diffraction peaks at 12.66°, 16.61°, 17.78°, 23.29°, 25.34°, 27.19°, 28.63°, 31.02°, 35.15°, 36.95°, 39.36° and 41.84°, which were attributed to the (001), (201), (201), (400), (002), (202), (202), (310), (600), (112), (203), and (511) crystal planes of a well-crystallized structure dominated by sodium metaphosphate ($NaPO_3$) phases, as confirmed by the reference (PDF #00-011-0650). Simultaneously, the presence of one broad peak at ~23.5° in the XRD image is attributed to the (002) crystal planes of amorphous carbon. Consequently, the combined XRD results suggest the successful preparation of PCMA-1, PCMA-7, and PCMA-11. In addition, FT-IR spectra further provided insights into the chemical bonding within the materials, as illustrated in Fig. 3b. Obviously, PCMA-1 displayed two strong absorption peaks at ~2900 cm^{-1} and ~1600 cm^{-1}, assigned to –CH and C=C, which indicates that PCMA-1 retained a partial organic structure and moderate graphitization. Additionally, PCMA-7 was found to have a reduction in –CH absorption but retained significant C=C stretching, suggesting an increase in carbon framework disorder in it. In comparison with PCMA-1 and PCMA-7, PCMA-11 displayed the weakest –CH and C=C peaks but the strongest C–O peak at ~1100 cm^{-1}, indicating extensive oxidation and defect formation. The presence of oxygen-containing functional groups enhanced surface hydrophilicity and catalytic activity by promoting reactant adsorption and electron transfer. As expected, PCMA-7 had an excellent catalytic performance for UOR. In order to quantify the differences in structural properties and defect sites in the catalysts, Raman spectroscopy was used to characterize PCMA-1, PCMA-7, and PCMA-11. As shown in Fig. 3c, the three samples exhibited two obvious characteristic D bands and G bands at about 1350

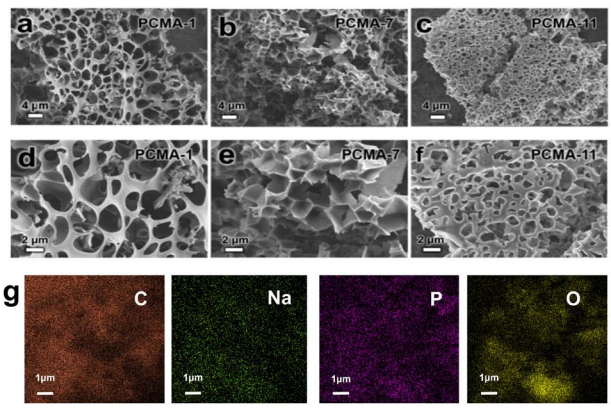

Fig. 2 Low-magnification SEM images of (a) PCMA-1, (b) PCMA-7 and (c) PCMA-11. High-magnification SEM image of (d) PCMA-1, (e) PCMA-7 and (f) PCMA-11. (g) EDS elements mapping images of PCMA-7 with the corresponding elements: C, O, Na and P.

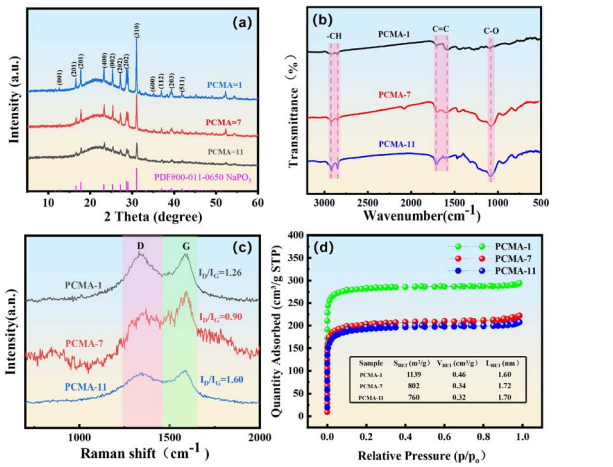

Fig. 3 (a) XRD patterns, (b) FT-IR spectra, (c) Raman spectra and (d) BET isotherms and the textural properties of PCMA-1, PCMA-7 and PCMA-11.

and 1580 cm^{-1}, respectively. As is well known that the D band represents defect-induced vibrations, while the G band corresponds to graphitic vibrations. The D and G band ratio (I_D/I_G) was employed to characterize the carbon material.[44] The lower the I_D/I_G value, the higher the degree of graphitization. Clearly, the I_D/I_G value of PCMA-7 was 0.90, lower than those of PCMA-1 (1.26) and PCMA-11 (1.60). Accordingly, PCMA-7 achieved the highest degree of graphitization, which was favorable for its higher electron conductivity and active site availability, thereby boosting its UOR. Besides, the mesoporosity of PCMA-1, PCMA-7, and PCMA-11 was further tested through N_2 adsorption–desorption measurements, and the as-obtained isotherms are displayed in Fig. 3d. Interestingly, it could be clearly seen that the three samples showed the adsorption isotherms representative of type IV isotherms with a H1-type hysteresis loop in good agreement with the IUPAC classification. Therefore, they were characteristic of mesoporous materials with ordered pore structures. As the inset table shows in Fig. 3d, the specific surface area of PCMA-7 was found to be 802 $m^2\ g^{-1}$, with a pore volume of 0.34 $cm^3\ g^{-1}$, and a pore size distribution centered at 1.72 nm. In contrast, PCMA-1 and PCMA-11 exhibited higher (1139 $m^2\ g^{-1}$) and lower (760 $m^2\ g^{-1}$) specific surface areas, respectively, with pore size distributions centred at 1.6 nm and 1.7 nm and pore volumes of 0.46 $cm^3\ g^{-1}$ and 0.32 $cm^3\ g^{-1}$, respectively. Although PCMA-7 did not possess the highest specific surface area and pore volume, it had the highest pore size distribution. This phenomenon suggests the presence of abundant irregular microporous and mesoporous structures in the carbon layers of the porous carbon materials, in agreement with the microscopic morphology observed by SEM. This range of distribution data is of great significance for the adsorption performance and gas transport properties of the material.

The significant differences in surface chemical composition, bonding state and functional group distribution also plays a key role in influencing the electrochemical properties of the materials. Therefore, XPS measurements were conducted to further confirm the chemical states of the elements in PCMA-1, PCMA-7 and PCMA-11, and their corresponding XPS spectroscopic results are shown in Fig. 4a–c. Obviously, concerning the carbon skeleton structure, it was found that the deconvoluted C 1s spectra (Fig. 4a) exhibited similar peak structures for all three samples. The characteristic peak at 284.8 eV corresponds to the graphitized carbon skeleton (C=C), while peaks in the 286.0–286.4 eV and 288.8–288.9 eV regions are attributed to C–O and C=O bonds, respectively. It is noteworthy that the C–O bond energy (286.41 eV) in the PCMA-1 sample displayed a marked positive shift, indicating that the acidic preparation environment fostered the formation of C–O–P bonding structures. Deconvolution of the phosphorus (P) 2p spectra (Fig. 4b) of all samples revealed the presence of characteristic double peaks at 134.56 eV (P $2p_{3/2}$) and 135.5–135.6 eV (P $2p_{1/2}$), thereby confirming the successful anchoring of phosphate ester functional groups, which are dominated by P=O structures. It is worth noting that the P $2p_{1/2}$ binding energy (135.61 eV) in the PCMA-7 sample displayed a marginal positive shift in comparison to other samples. This directly reflects how neutral preparation conditions induced specific changes in the electronic structure of the P=O bond, resulting in higher electron binding energy. In addition, the oxygen analysis provided fundamental evidence for understanding the performance differences in UOR. The fitting of the O 1s spectrum (Fig. 4c) revealed two primary oxygen species: the O(1) component at 530.8–530.9 eV (assigned to P=O bonds and surface-adsorbed oxygen) and the O(2) component at 532.0–532.2 eV (corresponding to carbon–oxygen bonds near defect sites). The data presented in Fig. 4d suggest that PCMA-7 demonstrates the highest relative defect oxygen content (67.11%), which was significantly higher than those observed in PCMA-1 (61.35%) and PCMA-11 (59.17%). This finding suggests that a precursor pH of 7 is most favorable to creating high-density defect structures within the carbon matrix.

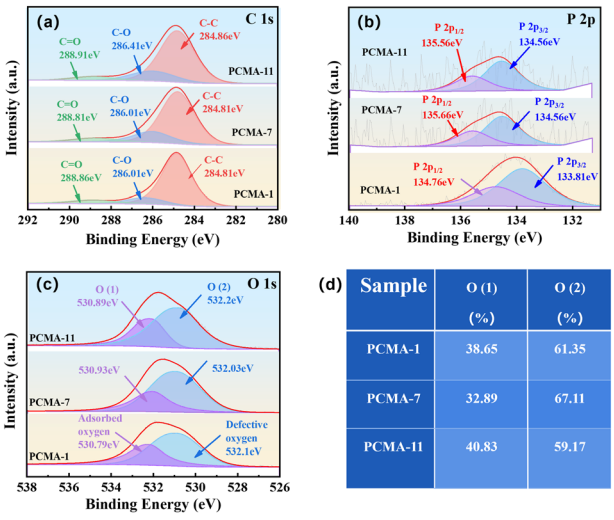

Fig. 4 XPS spectra of (a) C 1s, (b) P 2p, and (c) O 1s, (d) the percentage of O(1) to O(2) in PCMA-1, PCMA-7 and PCMA-11, respectively.

The exceptional UOR performance exhibited by the PCMA-7 sample is predominantly ascribed to its distinctive surface electronic structure and high density of active sites. In addition, the neutral environment has been shown to induce the formation of P=O functional groups, which possess a more electron-deficient electronic structure. This characteristic enhances its affinity for and activation capability of the $-NH_2$ group in electron-rich urea molecules. Conversely, and more pertinently, the PCMA-7 sample demonstrates a substantial enrichment of structural defects (as illustrated by O(2)). These defect sites themselves serve as highly active centres for urea molecule adsorption and conversion, and their high density directly enhances the material's intrinsic catalytic activity. It can thus be concluded that the discrepancy in UOR performance is principally determined by variations in the concentration of defect oxygen within the carbon framework. Concurrently, the electronic state modulation of the P=O functional group provided supplementary performance optimisation.

To further explore the electrocatalytic UOR performance of the as-prepared catalysts, their electrocatalytic UOR activities were tested and then compared in a mixed electrolyte containing 1.0 M KOH + 0.33 M urea. The polarization curves (Fig. 5a) clearly confirm that PCMA-7 delivered the lowest potential at 10

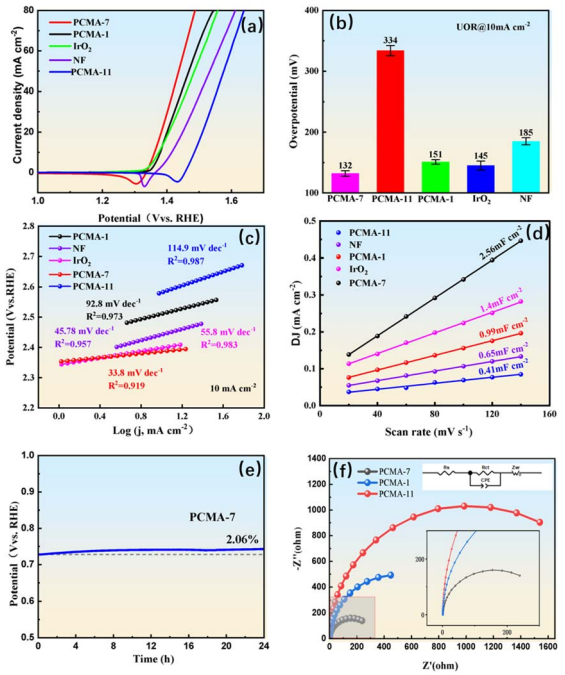

Fig. 5 (a) LSV curves of porous carbon materials. (b) Overpotential histogram. (c) Tafel slope of porous carbon materials. (d) C_{dl} curves of PCMA-1, PCMA-7, PCMA-11, NF, and IrO_2. (e) Stability of UOR catalysis. (f) EIS plots for PCMA-1, PCMA-7 and PCMA-11.

mA cm^{-2}, outperforming PCMA-1, PCMA-11, NF and even the benchmark catalyst IrO_2 at the same current density. In order to carefully evaluate the difference in their electrocatalytic performance for UOR, their corresponding overpotentials at 10 mA cm^{-2} were obtained from the polarization curves, as shown in Fig. 5a. PCMA-7, PCMA-11, PCMA-1, IrO_2 and NF gave the overpotentials of 132, 334, 151, 145, and 185 mV at 10 mA cm^{-2}, respectively. Fig. 5b illustrates the difference in overpotential between PCMA-7 and IrO_2. Error bars are included in the bar chart; the range of error represents the standard deviation from three independent replicate experiments. The inclusion of error bars clearly demonstrates a statistically significant difference between PCMA-7 and IrO_2, confirming that PCMA-7 exhibited superior electrocatalytic activity than conventional IrO_2 electrodes under the same conditions. In addition, their corresponding Tafel slopes were obtained from CV curves and further compared to assess the UOR reaction kinetics of the electrocatalysts. Fig. 5c shows the Tafel curves for catalysts such as PCMA-1, NF, IrO_2, PCMA-7, and PCMA-11. To avoid distorting the kinetic interpretation by extracting slopes from the initial potential region of the reaction, only the significant kinetic region (>1.3 V *vs.* RHE) was linearly fitted in the figure. The R^2 values for the linear fits were all greater than 0.95, with the slope values being: PCMA-11 114.9 mV dec^{-1}, PCMA-1 92.8 mV dec^{-1}, NF 45.78 mV dec^{-1}, IrO_2 55.8 mV dec^{-1}, and PCMA-7 33.8 mV dec^{-1}. Based on the combined results of LSV curves, overpotentials and Tafel plots, the PCMA-7 electrode shows a remarkable UOR activity and improved UOR reaction kinetics.

Furthermore, their corresponding electrochemical active surface area (ECSA) was determined from double-layer capacitance (C_{dl}) measurements to reveal the intrinsic activity of the catalysts in the range of non-faradaic potential C_{dl}. The electrochemical double-layer capacitance (C_{dl}) (Fig. 5d) served as an indicator of ECSA, which was directly linked to the number of accessible catalytic sites. PCMA-7 demonstrated the highest C_{dl} value (2.5 mF cm^{-2}), indicative of its significantly larger active surface area than the other samples. This feature was critical in facilitating higher catalytic activity, as more active sites were available to participate in the OER process. In comparison, PCMA-1 (1.4 mF cm^{-2}) and IrO_2 (0.995 mF cm^{-2}) showed moderate values, while the capacitances of PCMA-11 (0.465 mF cm^{-2}) and NF (0.652 mF cm^{-2}) were much smaller, reflecting their limited active site availability.

Firstly, the BET specific surface area reflected the total physical surface area of a material; however, the ultramicroporous pores smaller than 0.5 nm were difficult for the electrolyte to wet or presented extremely high resistance to ion transport, rendering this portion of the surface 'inactive' in electrochemical testing. PCMA-7 had a pore size of 1.72 nm, which was more conducive to the diffusion of hydrated ions, forming an efficient ion transport network; consequently, its physical surface area utilization was significantly higher than that of PCMA-1.[45] Secondly, the electrochemically active area was assessed *via* the double-layer capacitance (C_{dl}). PCMA-7 exhibited a higher C_{dl} value, indicating that more intrinsic active sites were distributed per unit physical area; this may be related to its surface electronic structure or atomic arrangement, which was more conducive to double-layer formation.[46] Consequently, although its physical surface area was smaller, its 'active site density' is extremely high. In summary, PCMA-7 overcame the drawback of poor microporous wettability thanks to its optimal pore size of 1.72 nm, and possessed a high density of intrinsic active sites, resulting in a larger effective surface area in practical electrochemical environments and consequently a higher measured C_{dl} value. The exceptionally high C_{dl} of PCMA-7 suggested that its structure not only enlarged the surface area but also optimized the accessibility and utilization of catalytic sites. This attribute, combined with its superior kinetic performance and low overpotential, underscores the value of PCMA-7 as a transformative material and a valuable candidate for practical implementation in UOR for the issue of urea-containing wastewater to produce hydrogen and address environmental pollution.

According to the long-term stability data for the PCMA-7 catalyst (Fig. 5e), the current increased by only 2.06% over a 24-hour period during the UOR test, indicating that the PCMA-7 catalyst has an extremely stable performance throughout its electrocatalytic UOR process. Fig. 5f showed the electrochemical impedance spectroscopy (EIS) results for three samples with different formulations (PCMA-7, PCMA-1, and PCMA-11). The figure presented a Nyquist plot, with the real part of the complex impedance (Z') on the horizontal axis and the negative of the imaginary part of the complex impedance ($-Z''$) on the vertical axis; all data points were located in the fourth quadrant.[47–49] The experimentally measured impedance

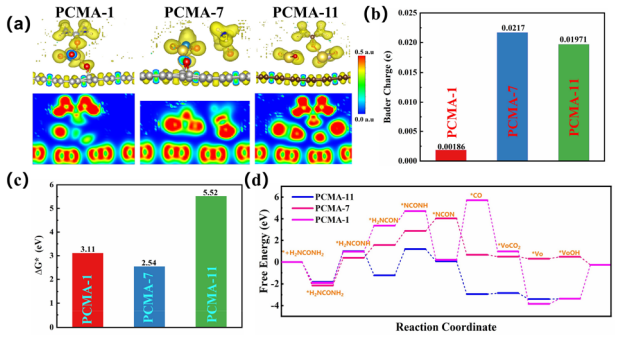

Fig. 6 (a) Charge density difference maps, (b) Bader charge analysis calculations, (c) adsorption energy calculations, and (d) free energy calculations for PCMA-1, PCMA-7, and PCMA-11 during the entire UOR process.

points (circles) for each sample and their corresponding equivalent circuit fitting curves (solid lines) were clearly visible. It could be seen from the figure that the PCMA-7 sample had the smallest semicircular radius, indicating the lowest charge transfer resistance (R_{ct}) and the highest electrochemical activity; whereas the PCMA-11 sample had the largest semicircular diameter, a higher R_{ct}, and restricted charge transfer kinetics.

More importantly, in order to unveil the electrocatalytic UOR mechanism of PCMA-7, DFT calculations were conducted. The charge density maps (Fig. 6a) displayed the electron redistribution on the surface of PCMA-1, PCMA-7, and PCMA-11. According to Fig. 6a, the behavior of the electron transfer was obtained, as displayed in Fig. 6b. It could be clearly observed that the urea molecular on PCMA-1 and PCMA-11 gave electron transfer values of 0.00186 and 0.01971, respectively, which were lower than that on PCMA-7, due to the highest oxygen vacancies within PMCA-7 to assist $NaPO_3$ in efficiently facilitating urea transfer in the catalytic process. In addition, it was obvious that PCMA-1 and PCMA-11 showed energy barriers of 3.11 eV and 5.52 eV for the rate-determining step (RDS) at the potential of 1.23 V, respectively. Whereas, PCMA-7 was able to further reduce the free energy gap of RDS to 1.80 eV when the potential was fixed (Fig. 6c). These theoretical results definitively verified that the oxygen vacancies within PCMA-7 effectively helped $NaPO_3$ reduce the thermodynamic UOR barriers for improving catalytic activity in critical processes. To accurately investigate the role of oxygen vacancies for $NaPO_3$ to boost the UOR performance, the Gibbs free energy of UOR pathways, furthermore, was calculated, as displayed in Fig. 6d. Obviously, the urea molecule was firstly adsorbed on the corresponding active sites, and then the four hydrogen atoms were continuously removed from the urea molecule and in theory CO_2 and N_2 were finally released. During the entire UOR process, PCMA-7 delivered lower free energy than those of PCMA-1 and PCMA-11. This substantial reduction reveals that the presence of oxygen vacancies strengthens intermediate adsorption and activation, while $NaPO_3$ accelerates the reaction of key intermediates through lone-pair interactions, thereby leading to superior electrocatalytic efficiency for UOR.

4. Conclusions

In summary, biomass was obtained from CPLB using the acid precipitation method after its pH value (pH = 1, 7, and 11) was adjusted by H_3PO_4. Porous carbon supporting $NaPO_3$ (PCMA-x, x = 1, 7, and 11) were successfully prepared after being treated at high temperature. Experimental results confirmed that PCMA-7 delivered the highest catalytic UOR performance with the overpotential of only 132 mV at 10 mA cm^{-2} and the lowest Tafel slope of 33.8 mV dec^{-1}. Theoretical results confirmed that the highest electrocatalytic UOR performance was due to (1) the porous structure that gave sufficient channels for ion transport/electrolyte transmission to help them more accessibly come into contact with active sites in PCMA-7; (2) abundant oxygen vacancies redistributed the local charge density to strengthen intermediate adsorption/activation, thus reducing the reaction energy barrier during the RDS process; (3) PO_3^- in PCMA-7 was able to promote interactions with intermediates to improve the electrocatalytic UOR reaction. Therefore, this work provides an efficient strategy for converting CPBL into cost-effective electrocatalysts for the efficient treatment of urea-rich wastewater.

Author contributions

Zhuoyan Liu: data curation. Haowen Li: writing – original draft. Zhenming Li: formal analysis. Yixin Zheng: data curation. Raojie Liao: formal analysis. Jianfeng Li: validation. Lijun Wang: visualization. Jianhui Jiang: supervision. Libing Hu: conceptualization and writing – review and editing. Jianbo Zhao: supervision and project administration.

Conflicts of interest

The authors declared no potential conflicts of interest with respect to the research, authorship and/or publication of this article.

Data availability

Data available on request from the authors.

Acknowledgements

This work was supported by the Natural Science Support Program of XPCC (no. 2024ZD104 and 2023AB033) and the Principal's Fund of Tarim University (no. TDZKCX202411).

Notes and references

1 S. J. Davis, N. S. Lewis, M. Shaner, S. Aggarwal, D. Arent, I. L. Azevedo, S. M. Benson, T. Bradley, J. Brouwer and Y.-M. Chiang, Net-zero emissions energy systems, *Science*, 2018, **360**, eaas9793, DOI: 10.1126/science.aas9793.
2 Z. W. Seh, J. Kibsgaard, C. F. Dickens, I. Chorkendorff, J. K. Norskov and T. F. Jaramillo, Combining theory and experiment in electrocatalysis: Insights into materials

design, *Science*, 2017, **355**, eaad4998, DOI: 10.1126/science.aad4998.

3 B. You and Y. Sun, Innovative strategies for electrocatalytic water splitting, *Acc. Chem. Res.*, 2018, **51**, 1571–1580, DOI: 10.1021/acs.accounts.8b00002.

4 Y. Shi, F. Tang, L. Liang, J. Zhu, J. Jiang, F. Bao, C. Shi, F. Yu and L. Hu, Constructing built-in electric field in heterogeneous interface of V_2O_5/MnFePBA for efficient oxygen evolution reaction and urea oxidation reaction, *Int. J. Hydrogen Energy*, 2025, **138**, 320–330, DOI: 10.1016/j.ijhydene.2025.05.185.

5 L. Nisar, M. Sadaqat, A. Hassan, N.-U.-A. Babar, A. Shah, M. Najam-Ul-Haq, M. N. Ashiq, M. F. Ehsan and K. S. Joya, Ultrathin CoTe nanoflakes electrode demonstrating low overpotential for overall water splitting, *Fuel*, 2020, **280**, 118666, DOI: 10.1016/j.fuel.2020.118666.

6 J. E. Lee, K.-J. Jeon, P. L. Show, I. H. Lee, S.-C. Jung, Y. J. Choi, G. H. Rhee, K.-Y. A. Lin and Y.-K. Park, Mini review on H_2 production from electrochemical water splitting according to special nanostructured morphology of electrocatalysts, *Fuel*, 2022, **308**, 122048, DOI: 10.1016/j.fuel.2021.122048.

7 F. Emiliana and T. J. Schmidt, Oxygen evolution reaction-the enigma in water electrolysis, *ACS Catal.*, 2018, **8**, 9765–9774, DOI: 10.1021/acscatal.8b02712.

8 S. Han, H. Li, T. Li, F. Chen, R. Yang, Y. Yu and B. Zhang, Ultralow overpotential nitrate reduction to ammonia via a three-step relay mechanism, *Nat. Catal.*, 2023, **6**, 402–414, DOI: 10.1038/s41929-023-00951-2.

9 X. Gao, S. Zhang, P. Wang, M. Jaroniec, Y. Zheng and S.-Z. Qiao, Urea catalytic oxidation for energy and environmental applications, *Chem. Soc. Rev.*, 2024, **53**, 1552–1591, DOI: 10.1039/d3cs00963g.

10 H. Wang, X. Li and C. Si, Electrocatalytic oxidation of biomass-derived chemicals using non-precious metal catalysts: design strategies, performance characteristics and perspectives, *Green Chem.*, 2025, **27**, 10346–10371, DOI: 10.1039/d5gc00719d.

11 A. N. Rollinson, J. Jones, V. Dupont and M. V. Twigg, Urea as a hydrogen carrier: a perspective on its potential for safe, sustainable and long-term energy supply, *Energy Environ. Sci.*, 2011, **4**, 1216–1224, DOI: 10.1039/c0ee00705f.

12 S. Xu, X. Ruan, M. Ganesan, J. Wu, S. K. Ravi and X. Cui, Transition metal-based catalysts for urea oxidation reaction (UOR): catalyst design strategies, applications, and future perspectives, *Adv. Funct. Mater.*, 2024, **34**, 2313309, DOI: 10.1002/adfm.202313309.

13 W. Sun, M. Zhang, J. Li and C. Peng, Solar-driven catalytic uurea oxidation for environmental remediation and energy recovery, *ChemSusChem*, 2022, **15**, e202201263, DOI: 10.1002/cssc.202201263.

14 M. A. Hefnawy, S. A. Fadlallah, R. M. El-Sherif and S. S. Medany, Synergistic effect of Cu-doped NiO for enhancing urea electrooxidation: comparative electrochemical and DFT studies, *J. Alloys Compd.*, 2022, **896**, 162857, DOI: 10.1016/j.jallcom.2021.162857.

15 C. Wang, A. Schechter and L. Feng, Iridium-based catalysts for oxygen evolution reaction in acidic media: mechanism, catalytic promotion effects and recent progress, *Nano Res. Energy*, 2023, **2**, e9120056, DOI: 10.26599/nre.2023.9120056.

16 X. Jia, H. Kang, X. Yang, Y. Li, K. Cui, X. Wu, W. Qin and G. Wu, Amorphous Ni(III)-based sulfides as bifunctional water and urea oxidation anode electrocatalysts for hydrogen generation from urea-containing water, *Appl. Catal., B*, 2022, **312**, 121389, DOI: 10.1016/j.apcatb.2022.121389.

17 S. Liu, S. Shang, L. Zhang, B. Cao, L. Meng, Y. Ding and H. Wu, Co_2P@MoO_3/NF composite as dual-functional electrocatalyst for energy-saving hydrogen production and urea oxidation, *Fuel*, 2024, **373**, 132362, DOI: 10.1016/j.fuel.2024.132362.

18 X. Gao, S. Zhang, P. Wang, M. Jaroniec, Y. Zheng and S.-Z. Qiao, Urea catalytic oxidation for energy and environmental applications, *Chem. Soc. Rev.*, 2024, **53**, 1552–1591, DOI: 10.1039/d3cs00963g.

19 P. Mei, J. Kim, N. A. Kumar, M. Pramanik, N. Kobayashi, Y. Sugahara and Y. Yamauchi, Phosphorus-based mesoporous materials for energy storage and conversion, *Joule*, 2018, **2**, 2289–2306, DOI: 10.1016/j.joule.2018.08.001.

20 M. Yang, Y. Jiang, M. Qu, Y. Qin, Y. Wang, W. Shen, R. He, W. Su and M. Li, Strong electronic couple engineering of transition metal phosphides-oxides heterostructures as multifunctional electrocatalyst for hydrogen production, *Appl. Catal., B*, 2020, **269**, 118803, DOI: 10.1016/j.apcatb.2020.118803.

21 Y. Zhang, J. Wu, B. Guo, H. Huo, S. Niu, S. Li and P. Xu, Recent advances of transition-metal metaphosphates for efficient electrocatalytic water splitting, *Carbon Energy*, 2023, **5**, e375, DOI: 10.1002/cey2.375.

22 B. Shen, Y. Feng, Y. Wang, P. Sun, L. Yang, Q. Jiang, H. He and H. Huang, Holey MXene nanosheets intimately coupled with ultrathin Ni-Fe layered double hydroxides for boosted hydrogen and oxygen evolution reactions, *Carbon*, 2023, **212**, 118141, DOI: 10.1016/j.carbon.2023.118141.

23 P. W. Menezes, C. Panda, C. Walter, M. Schwarze and M. Driess, A cobalt-based amorphous bifunctional electrocatalysts for water-splitting evolved from a single-source lazulite cobalt phosphate, *Adv. Funct. Mater.*, 2019, **29**, 1808632, DOI: 10.1002/adfm.201808632.

24 D. Li, C. Zhou, R. Yang, Y. Xing, S. Xu, D. Jiang, D. Tian and W. Shi, Interfacial engineering of the Co_xP-Fe_2P heterostructure for efficient and robust electrochemical overall water splitting, *ACS Sustainable Chem. Eng.*, 2021, **9**, 7737–7748, DOI: 10.1021/acssuschemeng.0c09377.

25 Y. Dong, X. Chen, B. Yu, W. Zhang, X. Zhu and Z. Liu, Engineering of P vacancies and phosphate on Fe-doped Ni_2P nanosheet arrays for enhanced oxygen evolution, *J. Alloys Compd.*, 2022, **905**, 164023, DOI: 10.1016/j.jallcom.2022.164023.

26 Y. Yu, J. Li, J. Luo, Z. Kang, C. Jia, Z. Liu, W. Huang, Q. Chen, P. Deng and Y. Shen, Mo-decorated cobalt phosphide nanoarrays as bifunctional electrocatalysts for efficient overall water/seawater splitting, *Mater. Today Nano*, 2022, **18**, 100216, DOI: 10.1016/j.mtnano.2022.100216.

27 R. Gond, D. K. Singh, M. Eswaramoorthy and P. Barpanda, Sodium cobalt metaphosphate as an efficient oxygen evolution reaction catalyst in alkaline solution, *Angew. Chem.*, 2019, **58**, 8330–8335, DOI: 10.1002/ange.201901813.

28 M. B. Gawande, P. Fornasiero and R. Zboril, Carbon-based single-atom catalysts for advanced applications, *ACS Catal.*, 2020, **10**, 2231–2259, DOI: 10.1021/acscatal.9b04217.

29 J. Wang, J. Kim, S. Choi, H. Wang and J. Lim, A review of carbon-supported nonprecious metals as energy-related electrocatalysts, *Small Methods*, 2020, **4**, 2000621, DOI: 10.1002/smtd.202000621.

30 Z. Liu, B. Li, Y. Feng, D. Jia, C. Li, Q. Sun and Y. Zhou, $Ni(PO_3)_2$/CNTs hybrid architecture via phthalocyanine modulated self-assemblies for efficient hydrogen evolution reaction, *Appl. Surf. Sci.*, 2022, **571**, 151384, DOI: 10.1016/j.apsusc.2021.151384.

31 C. Zhu, H. Li, S. Fu, D. Du and Y. Lin, Highly efficient nonprecious metal catalysts towards oxygen reduction reaction based on three-dimensional porous carbon nanostructures, *Chem. Soc. Rev.*, 2016, **45**, 517–531, DOI: 10.1039/c5cs00670h.

32 H. Jiang, Y. Wang, J. Hao, Y. Liu, W. Li and J. Li, N and P co-functionalized three-dimensional porous carbon networks as efficient metal-free electrocatalysts for oxygen reduction reaction, *Carbon*, 2017, **122**, 64–73, DOI: 10.1016/j.carbon.2017.06.043.

33 M. Belluati, S. Tabasso, E. C. Gaudino, G. Cravotto and M. Manzoli, Biomass-derived carbon-based catalysts for lignocellulosic biomass and waste valorisation: a circular approach, *Green Chem.*, 2024, **26**, 8642–8668, DOI: 10.1039/d4gc00606b.

34 Y. Zhang, Q. Fu, B. Song and P. Xu, Regulation strategy of transition metal oxide-based electrocatalysts for enhanced oxygen evolution reaction, *Acc. Mater. Res.*, 2022, **3**, 1088–1100, DOI: 10.1021/accountsmr.2c00161.

35 X. Wei, C. Chen, X. Z. Fu and S. Wang, Oxygen vacancies-rich metal oxide for electrocatalytic nitrogen cycle, *Adv. Energy Mater.*, 2024, **14**, 2303027, DOI: 10.1002/aenm.202303027.

36 Y. Zhai, X. Ren, Y. Sun, D. Li, B. Wang and S. F. Liu, Synergistic effect of multiple vacancies to induce lattice oxygen redox in NiFe-layered double hydroxide OER catalysts, *Appl. Catal., B*, 2023, **323**, 122091, DOI: 10.1016/j.apcatb.2022.122091.

37 D. Wang, F. Tang, H. Bai, P. Wu, Y. Zhang, L. Fang, B. Sun, C. Shi and L. Hu, Ce dopant regulating oxygen vacancy of medium-entropy NiCoFe-LDH for efficiently enhancing urea-assisted electrolytic hydrogen production, *J. Alloys Compd.*, 2025, **1014**, 178660, DOI: 10.1016/j.jallcom.2025.178660.

38 M. Sun, H. Liu, J. Qu and J. Li, Earth-rich transition metal phosphide for energy conversion and storage, *Adv. Energy Mater.*, 2016, **6**, 1600087, DOI: 10.1002/aenm.201600087.

39 Q. Li, Y. Wang, T. Pan, Y. Zhu and H. Pang, Ni-based electrocatalysts for urea oxidation reaction: mechanism, catalyst design strategies and future perspectives, *Sci. China Mater.*, 2025, **68**, 317–340, DOI: 10.1007/s40843-024-3207-1.

40 Y. Qin, L. Miao, M. Mansuer, C. Hu, Y. Lv, L. Gan and M. Liu, Spatial confinement strategy for micelle-size-mediated modulation of mesopores in hierarchical porous carbon nanosheets with an efficient capacitive response, *ACS Appl. Mater. Interfaces*, 2022, **14**, 33328–33339, DOI: 10.1021/acsami.2c08342.

41 Y. Tong, P. Chen, M. Zhang, T. Zhou, L. Zhang, W. Chu, C. Wu and Y. Xie, Oxygen vacancies confined in nickel molybdenum oxide porous nanosheets for promoted electrocatalytic urea oxidation, *ACS Catal.*, 2018, **8**, 1–7, DOI: 10.1021/acscatal.7b03177.

42 L. Hu, Q. Zhu, Q. Wu, D. Li, Z. An and B. Xu, Natural biomass-derived hierarchical porous carbon synthesized by an in situ hard template coupled with NaOH activation for ultrahigh rate supercapacitors, *ACS Sustainable Chem. Eng.*, 2018, **6**, 13949–13959, DOI: 10.1021/acssuschemeng.8b02299.

43 Y. G. Guo, J. S. Hu and L. J. Wan, Nanostructured materials for electrochemical energy conversion and storage devices, *Adv. Mater.*, 2008, **20**, 2878–2887, DOI: 10.1002/adma.200800627.

44 A. C. Ferrari and D. M. Basko, Raman spectroscopy as a versatile tool for studying the properties of graphene, *Nat. Nanotechnol.*, 2013, **8**, 235–246, DOI: 10.1038/nnano.2013.46.

45 A. Sedighi, E. Hassanizadeh, R. Abedi, A. Talebi, S. E. Faz, N. Rahimpanah, T. Hosseinzadeh and G. B. Darband, High-abundant active sites Co-Mn-Se@Ni_3S_2 binder-free heterojunction electrocatalyst for energy-saving electrochemical hydrogen production, *Electrochim. Acta*, 2025, 147221, DOI: 10.1016/j.electacta.2025.147221.

46 S. Khademjafari, A. S. Rouhaghdam, D. Iravani, A. Talebi, G. B. Darband and S. Shanmugam, Binder-free Co-P@Ni-Cu cedar leaf-like hierarchical structure as an efficient and stable electrocatalyst for hydrogen and oxygen evolution reactions, *J. Power Sources*, 2026, **661**, 238608, DOI: 10.1016/j.jpowsour.2025.238608.

47 A. Talebi and G. B. Darband, Ultra-fast one-step electrochemical synthesize of Ni-Mn-P as an active and stable electrocatalyst for green hydrogen production, *Fuel*, 2025, **397**, 135427, DOI: 10.1016/j.fuel.2025.135427.

48 S. Amanian, A. Talebi and G. B. Darband, Facile and Fast Dynamic Hydrogen Bubble Temple Electrodeposition of Quaternary Phosphide Nanostructures for Energy-saving Hydrogen Production, *Electrochim. Acta*, 2025, 147681, DOI: 10.1016/j.electacta.2025.147681.

49 A. Talebi, G. B. Darband, M. Mirjalili and J. Li, Synergistic engineering of a dendritic Ni-Cu-Co-P electrocatalyst via a dynamic hydrogen bubble template for efficient and durable bifunctional water splitting, *J. Mater. Chem. A*, 2026, **14**, 8895–8912, DOI: 10.1039/d5ta06673e.